Dalton Transactions

Accepted Manuscript

ROYAL SOCIETY OF CHEMISTRY

www.rsc.org/dalton

Journal Name

RSCPublishing

ARTICLE

Morphology Control of the Perovskite Film for Efficient Solar Cells

Cite this: DOI: 10.1039/x0xx00000x

Lingling Zheng,[a] Danfei Zhang,[a] Yingzhuang Ma,[a] Zelin Lu,[a] Zhijian Chen,[a,b,c] Shufeng Wang,[a,c] Lixin Xiao,[a,b,c]* and Qihuang Gong[a]

Received 00th January 2012,
Accepted 00th January 2012

DOI: 10.1039/x0xx00000x

www.rsc.org/

In the past two years, the power conversion efficiency (PCE) of organic-inorganic hybrid perovskite solar cells has significantly increased up to 20.1%. These state-of-the-art new devices surpass other third-generation solar cells and become the most promising rival to the silicon-based solar cells. Since the morphology of the perovskite film is one of the most crucial factors to affect the device performance, many approaches were developed to make the improvement. This review provides a systematical summary on the methods of morphology control. The introductions and discussions on the mechanism and relevant hotspots are also given. Understanding the growth process of perovskite crystallites has great benefit for further efficiency improvement and enlightens us to exploit new technologies for large-scale, low-cost and high-performance perovskite solar cells.

1. Introduction

During the past two decades, inorganic-organic hybrid perovskite was investigated enthusiastically due to its excellent optical and electronic properties.[1-3] The hybrid perovskite has a formula ABX_3, where X is usually a halogen ion (I^-, Br^-, Cl^-), A is an organic ammonium ion (e.g. $CH_3NH_3^+$, $NH{=}CHNH_3^+$) and B is Pb^{2+} or Sn^{2+} (Figure 1). The corners of the cube were occupied by the small organic cations, so that a three-dimensional (3D) framework could form with arrays of corner-sharing metal halide octahedra, resulting in a narrow band gap.[1,4-6] For example, the most popular $CH_3NH_3PbI_3$ and $CH_3NH_3PbI_{3-x}Cl_x$ have a direct band gap of ~1.55 eV, corresponding to an absorption onset of 800 nm and intense absorption of the whole visible region.[7-9] Through regulating the ions, tunable properties can be obtained with extended absorption in the near-infrared region.[10-14] Moreover, the exciton binding energy of these perovskites is very small relative to the organic semiconductor, corresponding to the long exciton diffusion length of 100-1000 nm and lifetime of ~100 ns.[15-18] All these advantages promise the great potential of the hybrid perovskite as the light absorber for new-generation solar cells.

Although found decades ago, perovskite was firstly used as the light absorber for liquid dye-sensitized solar cells in 2009 by Miyasaka et al with a power conversion efficiency (PCE) of only 3.8%.[19] The PCE and the device stability were significantly enhanced by replacing the liquid hole transporting material (HTM) with the solid 2,2',7,7'-tetrakis(*N*,*N*-di-*p*-methoxyphenylamine)-9,9'-spirobifluorene (Spiro-OMeTAD) to avoid the dissolution of perovskite.[20-31] In 2012, a solid-state mesoscopic solar cell based on $CH_3NH_3PbI_3$ by solution process was fabricated with a PCE of 9.7%.[32] Snaith et al drived the PCE to 10.9% by replacing the mesoporous TiO_2 with Al_2O_3 as a scaffold.[33] They also successfully fabricated the perovskite solar cells (PSCs) without mesoporous layer via carefully morphology optimizing.[34] Grätzel et al exploited a two-step sequential deposition method, demonstrating a much uniform morphology as well as a high PCE of above 15%.[35] Y. Yang et al reported a planar PSC with a PCE of 19.3% by efficient interface engineering.[36] Recently, the certified PCE of the PSC have been boosted up to 20%, which is the most promising rival to the silicon-based solar cells (Figure 1).[37]

One of the most crucial issues for PSCs is the morphology control of the perovskite film. Many photo-physical properties, such as light harvesting, charge carrier transport and diffusion length can be dramatically affected by the crystallization of the perovskite.[21,34,38-40] The defects and the crystal grain boundaries of the perovskite crystallites act as the traps of carriers, which would aggravate the charge recombination. The hysteresis effect, which causes the inaccuracy in evaluating cell efficiency, is also believed to be related to the crystallinity and interfaces of the perovskite.[41-45] Thus, the device performance strongly depends on the morphology of the perovskite film.

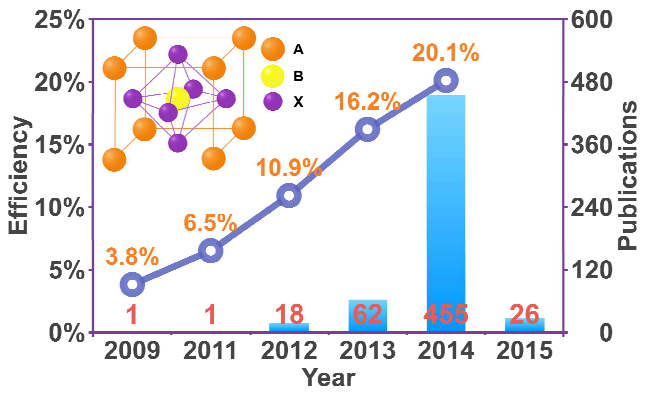

Figure 1. The publications and efficiency evolution of the perovskite solar cells (updated to 2015.02.01). The insertion is the crystal structure of inorganic-organic hybrid perovskite ABX_3 with cubic symmetry.

Two architectures of PSCs were researched most commonly: the meso-structured device and the planar device (Figure 2). The growth process of perovskite crystallites in these two kinds of devices differs greatly. The meso-structured device generally employed a layer of hundreds-nanometer-thick mesoporous TiO_2 or Al_2O_3 as the scaffold, so that the crystallization of the perovskite greatly benefits from the enhanced nucleation at the mesostructure surface. The pore filling and the homogeneity of the perovskite layer should be concerned for this architecture during the film formation, and a capping layer of perovskite with suitable thickness on the mesocopic structure was verified to be beneficial for the device performance.[42,46-49] The planar device has a p-i-n junction, in which the perovskite is directly deposited on a compact n-type inorganic oxide or p-type PEDOT:PSS film, then covered by a solid organic HTM or fullerene electron acceptor, respectively. Owing to the simpler structure, a high-temperature (500°C) sinter process became no longer necessary for the planar architecture, which seems to be more attractive for practical application. However, it sets a challenge to control the morphology of perovskite films due to the lack of scaffold..[34] A fully covered dense layer of perovskite with large crystal grain size is very important for planar device to gain efficient light absorption and reduce the energy loss in the charge transport and collection process.[34,40,50-52]

According to the architectures, diverse film formation technologies, including one-step spin-coating deposition,[34,46] sequential deposition method,[35] two-step spin-coating deposition[53] and vapor deposition[54,55] were developed for efficient PSCs. In this review, we systematically summarized and compared the morphology control methods for the perovskite crystallites by different film formation technologies. Many key studies and findings are highlighted and discussed. A comprehensive understanding of the nucleation and the growth process of perovskite crystallites will guide us to further optimize the morphology and the efficiency of PSCs. In addition, the present studies on crystallites growth will enlighten us to master the morphology control of the perovskite film in a large-scale application, and explore new practical methods for large-scale, low-cost and high-performance PSCs.

2. One-step Spin-coating Method

One-step spin-coating method (Figure 3) is to spin coat a precursor solution of lead halide with a certain amount of the organic ammonium halide, and the perovskite crystallites then form and grow during the solvent evaporation. A post-annealing process at relatively high temperature (around 100°C) was usually required for fully crystallization of the perovskite and the removal of the residual solvents. For this method, the film morphology and the photovoltaic performance are very sensitive to the conditions and treatment, such as the annealing temperature,[34,38] the solution concentration,[48,56] precursor composition[50,51] and solvent choice.[57-59]

Generally, $CH_3NH_3PbI_3$ comes from a solution containing stoichiometric PbI_2 and methylammonium iodine (MAI), while $CH_3NH_3PbI_{3-x}Cl_x$, comes from nonstoichiometric $PbCl_2$ and MAI with a molar ratio of 1:3. Due to the higher formation energy of Cl-substituted $MAPbI_3$ compared to the triiodine type, the concentration of Cl^- is only allowed to be very low in the resultant perovskite.[9,60] The excess MAI can guarantee the molar ratio of Pb^{2+} and the halide is 1:3, since the redundant halide and methylammonium can evaporate during the annealing process. Many beneficial properties can be obtained using the mixed halides. For instance, the carrier diffusion length of $MAPbI_{3-x}Cl_x$ reaches 1000 nm, which is almost 10 times of that of $MAPbI_3$,[15-16] In addition, it was found that better moisture stability can be realized by incorporating Br^- and I^-.[61]

Lingling Zheng *is currently a Ph.D student at the Department of Physics, Peking University (China). She received her B.Sc degree in polymer science and engineering from Tsinghua University (Beijing, China) in 2010. Her current research interests are on perovskite solar cells.*

Lixin Xiao *is a professor of the Department of Physics, Peking University (China) since 2011. He received his Ph.D in applied chemistry from The University of Tokyo (Japan) in 2000. He has been working on organic optoelectronics materials and devices, especially on photovoltaic (PV) and organic light-emitting device (OLED).*

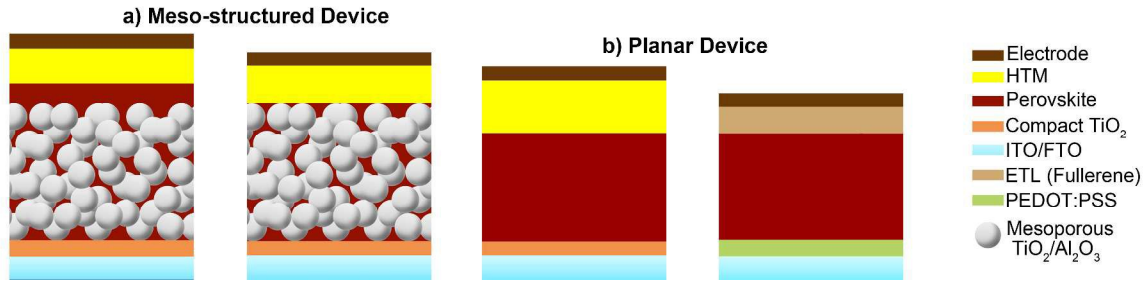

Figure 2. Structure diagram of a) the meso-structured perovskite solar cell and b) the planar perovskite solar cell.

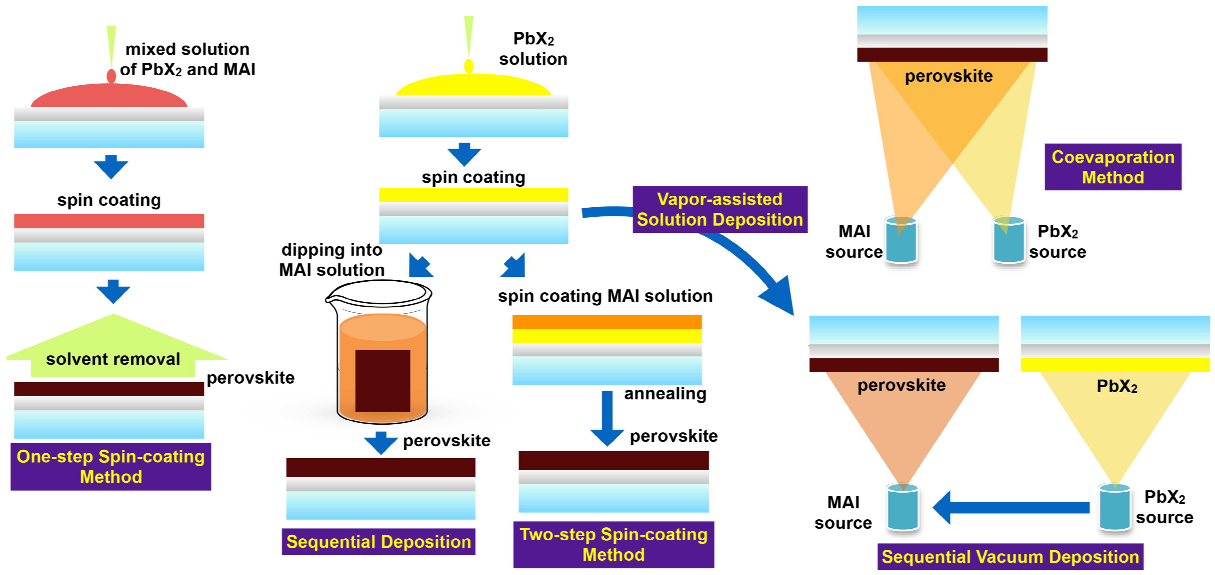

Figure 3. Schematic illustration of the diverse methods for perovskite solar cells.

Solvents (e.g. *N,N*-dimethylformamide (DMF) and *γ*-butyrolactone (GBL)) with good solubility of both lead halide and organic ammonium halide were frequently chosen for the device fabrication. It was found that $MAPbI_3$ from GBL solution preferred to form the clustered-domain morphology, while the interconnected needle-like crystalline was observed from a DMF precursor solution (Figure 4a,b).[35,58,62,63] Both films exhibited sparse surface coverage on the planar substrates without the mesoscopic structures. However, the surface coverage should be one of the most crucial factors to dominate the performance of planar devices, and an efficient PSC can be attained only with the high surface coverage.[34] The incomplete surface coverage of perovskite not only decreases the harvest of light by straight passing though the device, but also brings a lot of pinholes as the shunt paths for the direct contacts of the HTM and the electron transporting layer (ETL). All these caused simultaneous drops of the short-circuit current (J_{sc}), open-circuit voltage (V_{oc}), fill factor (*FF*) and the corresponding PCE. H. J. Snaith et al firstly confirmed the feasibility to form a perovskite film with nearly full coverage on a planar substrate by carefully control the annealing conditions.[34] It was demonstrated that the pores and the uncoverage increase with the crystal agglomerating and dewetting during annealing, which is driven by the evaporation of the solvent and mass. The evaporation rate can be slowed down under a relatively low annealing temperature of about 90°C on a film 450-550 nm, under which circumstances improved surface coverage was attained corresponding to a high PCE of 11.4% for $MAPbI_{3-x}Cl_x$ based PSCs (Figure 4c).[34] The phenomena that the coverage reduced with increasing annealing temperature was also observed by R. Tena-Zaere et al.[64] Y.-J. Hsu et al fabricated perovskite on a preheated NiO_x substrate at very high spinning speed to accelerate solvent evaporation and crystal formation,, which can reduce the coarsening of crystals.[65] As a result, surface coverage changed from 89% to 93% when the spinning speed increases from 8000 rpm to 9500 rpm. The sensitive dependence of the crystal growth on the environment upon annealing was investigated by

Y. Yang[66] and C. Surya et al[67]. An appropriate humidity environment (about 30%) provides a small amount of moisture within the grain boundaries, which helps grain boundary creep and the grain merge, giving rise to a film with reduced pinhole and large crystal grains beyond 500nm. This method produced the planar devices with a highest PCE of 17.1% base on the structure of ITO/ PEDOT:PSS/ $MAPbI_{3-x}Cl_x$/$PC_{61}BM$/PFN/Al.[66] Despite the annealing conditions, preheating of the substrate before spin coating,[62] rapidly quenching after annealing at high temperature[68] and a detailed temperature raising procedure[52,63] are also available to enhance the surface coverage and form a void-free perovskite films on the planar substrates.

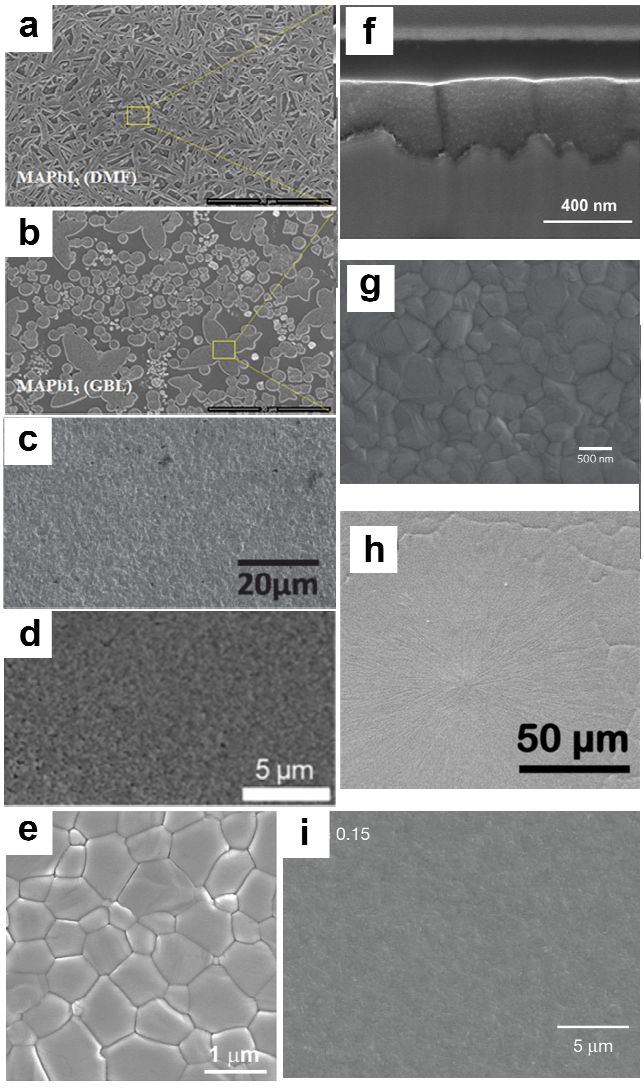

Figure 4. Representative top-view SEM images of the perovskite layer from a) DMF and b) GBL. Optimized perovskite films with a high coverage by c) controlling the annealing conditions, d) adding the additive and e) FDC method. f) The cross-sectional SEM image of the $MAPbI_3$ film fabricated by the FDC method. Representative top-view SEM images of the perovskite layer g) by solvent-engineering technology, h) by hot-casting technique at 180°C, i) containing $(FAPbI_3)_{0.85}(MAPbBr_3)_{0.15}$. a) and b) are reproduced from Ref. 58 with permission from American Chemical Society. c) is Reproduced from Ref. 34 with permission from Wiley-VCH. d) is reproduced from Ref. 71 with permission from The Royal Society of Chemistry. e) and f) are reproduced from Ref. 79 with permission from Wiley-VCH. g) is reproduced from Ref. 81 with permission from Nature Publishing Group. h) is reproduced from Ref. 85 with permission from Science(AAAS). i) is reproduced from Ref. 86 with permission from Nature Publishing Group.

Noting that the annealing process includes the conversion to perovskite, the effects of anneal temperature on the composition of the resultant film should also be investigated. For $MAPbI_3$ and $MAPbI_{3-x}Cl_x$, the conversion to perovskite requires a minimum temperature of 80°C.[38] The conversion of $MAPbI_3$ can be as fast as 10 min at 100°C, whereas the $MAPbI_{3-x}Cl_x$ need at least 45 min for sublimating the excessive mass.[38] Many literatures applied 100°C or above as the anneal temperature instead of the lower one at which the coverage would be better, might due to the much longer time required for conversion at low temperature.[64-69] Formamidinium lead triiodine ($FAPbI_3$) needs a much higher anneal temperature even above 150°C for a pure crystal phase and good device performance.[69,70] Thus, the selected temperature should be defined by the optimized surface morphology as well as the full conversion and crystallization of perovskite.

Making use of the additives into the precursor solution can effectively control the film formation process.[50,51,71-76] K. Zhu et al added MACl to the standard $MAPbI_3$ precursor solution, and found that pure $MAPbI_3$ formed with improved coverage and absorption on planar substrate. As a result, PCE increased from 2% to 12% for the planar cells and from 8% to 10% for the mesostructured cells.[51] The mechanism was illustrated as the existence of MACl slows down the crystallization of $MAPbI_3$ by producing some intermediate crystal structure, so the large elongated crystal turned into small crystals with a high surface coverage. Interestingly, after enough annealing time, no MACl was detected by EDX analysis, indicating all the Cl was sublimated and pure $MAPbI_3$ was formed.[51] L. Ding et al also confirmed the role of the ammonium chloride species using the MACl and NH_4Cl as the additives, and better performance was achieved using NH_4Cl to form a smoother film (Figure 4d).[71] Bidentate halogenated alkane as another sort of additives were developed to manipulate the crystallization rate of perovskite by temporarily chelating with the Pb^{2+} and releasing iodide during the thermal annealing.[50,72] A PCE of 12% was obtained from a p-i-n junction of PEDOT:PSS/ $MAPbI_{3-x}Cl_x$/$PC_{61}BM$ by adding a small amount of 1,8-diiodooctane (DIO), which can be attributed to a more uniform and continuous surface.[50] Further optimizations were taken on the alkyl chain length and the end halogens.[72] S. H. Im mixed HBr and H_2O into DMF to increase the solvent solubility of $MAPbBr_3$, so that the crystallization can be initiated at a higher concentration, leading to a denser crystal layer with high surface coverage.[73] An impressive PCE of 10.4% with a high V_{oc} of 1.51 V was achieved for $MAPbBr_3$ PSCs without significant hysteresis effect using a well-matched hole-transporting polymer.[73] Table 1 shows a summary of the reported additives and their performances.

Although the coverage problem can be circumvented by variable methods mentioned above, another challenge of the planar architecture is the balance of the light absorption and the charge collection efficiency.[77] On the one hand, the films

should be thick enough for sufficient light absorption to gain a high photogenerated current. On the other hands, if the film is much thicker than the diffusion length of the carrier, the charges would hardly reach the ETL or HTL interface to be collected, leading to a very low charge collection efficiency and *FF*. Computational studies attested that the performance of planar devices is strongly influenced by the thickness and defect density of the perovskite film.[78] A solar cell with a p-i-n of spiro-OMeTAD/$MAPbI_3$/TiO_2 was employed to investigate the effects of thickness by AMPS-1D simulation program. Based on a constant charge mobility of 50 cm^2/V-s , as the thickness was increased from 200 nm to 1000 nm, the calculated J_{sc} raised from 19.0 to 23.6 mA/cm^2 without obvious loss of V_{oc}.[78] But in the experiment, most of the planar devices can not perform well when the thickness reach the diffusion length of perovskite ($MAPbI_{3-x}Cl_x$ calculated as 1000 nm). This might be attributed to the massive charge traps produced during the crystal growth, which seriously stem the charge transport. The effect of the defect density on the device performance was also simulated, and the results demonstrated that increasing defect density in the bulk perovskite or interface would severely decrease the V_{oc} and PCE.[78] Hence, grain boundaries, always known as the enrichment regions of charge traps, should be eliminated across the carrier transport path. In other words, to expand the threshold thickness of the device as well as the charge mobility of the charge carriers, perovskite crystallites with a large grain size should be formed. So that, the least number of grain boundaries need to be passed through by the carriers before collected.

Above all, technologies aiming at a dense layer of large perovskite crystallites without reducing the surface coverage are highly desired. Based on this purpose, a fast deposition-crystallization (FDC) method was proposed by L. Spiccia and Y.-B. Cheng.[79] In this approach, the wet films from the standard $MAPbI_3$ solution were quickly exposured to a second poor solvent (chlorobenzene, toluene) of perovskite, followed by the DMF solvent extracted by the second solvent. Because of the rapidly reduced solubility of $MAPbI_3$ in the film, the supersaturation status drove quick uniform nucleation before the rapid growth of the crystal, a high-quality film of uniform micron-size grains with full surface coverage was produced (Figure 4e).[79] Subsequently, they reported a hot gas flow treatment which can also realize the supersaturation status at the early stage of crystallization.[80] As the SEM shown (Figure 4f), no grain boundaries parallel to the substrate was observed in a 350nm-thick film by this method, indicating the efficient carrier transport. S. I. Seok et al developed a solvent-engineering technology, which is suitable for both the planar and meso-structured devices.[81] A mixed solvent of dimethyl sulfoxide (DMSO) and GBL was used for the precursor and toluene was dripped onto the film during the spin-coating process.[58,81-84] When the toluene is introduced, a plate intermediate phase of MAI-PbI_2-DMSO was formed and converted to the perovskite phase finally.[81] The solid-state conversion mechanism refrained the crystals from over agglomeration during growth, yielding extremely uniform and flat films, whose morphology is quite similar to that by FDC method (Figure 4g). It is worthy to note that the hysteresis effects in the devices by FDC method or solvent-engineering technology attenuated obviously, revealing what a promising morphology should be like.

Quite recently, A. D. Mohite proposed a solution-based hot-casting technique, millimeter-scale leaf-like $MAPbI_{3-x}Cl_x$ single crystals were successfully produced to form a pinhole-free film (Figure 4h).[85] This technique calls for a hot (70°C) precursor solution of equivalent PbI_2 and MACl, which was spun coated on a hot substrate kept at the temperature of 180 °C. Because the substrate temperature is much higher than the crystallization temperature, excess solvent prolonged the crystals growth, yielding crystalline with the grain size of 1-2 mm. Hysteresis-free cells based on PEDOT:PSS/Perovskite/PCBM junction reached a PCE of 18%.[85] The PCE is only 9.1% when devices with small grains fabricated by a relatively low substrate temperature. Self-consistent optoelectronic simulation was performed to investigate the origin reasons for performance improvement. For small-grain device, the recombination mainly came from the bulk defects. When large-grain crystals were introduced, this part of recombination was remarkably suppressed. Different recombination processes were found in these two devices: for large-grain device, a dominated bimolecular recombination process represented the high crystalline quality; for small-grain device, the trap-assisted recombination was observed.[85] The conclusion was attested by the experimental results of time-resolved photoluminescence spectroscopy. Furthermore, the correlation of the mobility and the grain size was proposed. The mobility increased sharply with the crystal grain size, and for a 170 μm-size grain, the mobility can be as high as 20 cm^2/V-s.[85]

When compared to the planar architecture, the meso-structured devices didn't suffer much from the coverage problem and the rigid limitation of the device thickness, because the film forming was much improved and the carrier-collection efficiency can reach higher than 99% taking advantage of the mesoporous TiO_2 or Al_2O_3.[46,48,77] Instead, the pore filling is an important issue for the meso-structured architecture, which is dominated by the thickness of the mesoporous layer and the quantity of the perovskite deposited.[48] Therefore, a high concentration of the precursor solution (40 wt% for $MAPbI_3$, or 0.88M $PbCl_2$ + 2.64M MAI for $MAPbI_{3-x}Cl_x$) was usually used with adjusted thickness (300-400 nm) of the mesoporous layer.[38,46-49] Among the meso-structured devices, the best performance always come from those with a compact perovskite completely covered on the mesostructure and full pore filling.[48] The highest PCE of 16.7% was obtained from $MAPb(I_{1-x}Br_x)_3$ device with the capping layer by the solvent-engineering technology.[81] Since the coexistence of the compact perovskite capping layer and the mp-TiO_2 (Al_2O_3)/perovskite nanocomposite, the morphology control method used for the planar device can be also utilized for this architecture. S. I. Seok et al stabilized the crystal phase and modified the morphology of $FAPbI_3$ by incorporating 15% $MAPbBr_3$ (Figure 4i).[86] Low-gap $FAPbI_3$ offers a high J_{sc} and

$MAPbBr_3$ offers a large V_{oc} in the mesostructured cell based on $(FAPbI_3)_{0.85}(MAPbBr_3)_{0.15}$, yielding a high PCE of 18.4%.[86] Effective interface modification can be a useful method to control the crystal growth in the mesoscopic device. S. Hayase et al inserted HOCO-R-$NH_3^+I^-$ monolayer between the porous TiO_2 and perovskite. By anchoring TiO_2 and perovskite with $COOH^-$ and NH_3^+, HOCO-R-$NH_3^+I^-$ passivates the surface traps of TiO_2 and help to form large perovskite crystals.[87] HOCO-R-$NH_3^+I^-$ can also work as a dopant in $MAPbI_3$, by which a hole-conductor-free mesoscopic perovskite solar cell reached a high PCE of 12.8% with excellent stability.[88]

Table 1. A summary of the published performance for the perovskite solar cells with different additives by one-step spin-coating method.

Additive	Perovskite	Device	PCE (%)	Ref
		FTO/ bl-TiO_2/Perovskite /Spiro-OMeTAD /Au	12.10	51
CH_3NH_3Cl	$MAPbI_3$	FTO/ bl-TiO_2/mp- TiO_2:Perovskite /Spiro-OMeTAD /Au	10.09	51
		ITO/PEDOT:PSS/Perovskite/$PC_{61}BM$/Al	8.16	71
NH_4Cl	$MAPbI_3$	ITO/PEDOT:PSS/Perovskite/$PC_{61}BM$/Al	9.93	71
1,8-DIO	$MAPbI_{3-x}Cl_x$	ITO/ PEDOT:PSS/Perovskite/$PC_{61}BM$/Bis-C60/Ag	11.62/10.3	72/50
		FTO/ PEDOT:PSS/Perovskite/$PC_{61}BM$/Bis-C60/Ag	11.8	50
1,4-DIB	$MAPbI_{3-x}Cl_x$	ITO/ PEDOT:PSS/Perovskite/$PC_{61}BM$/Bis-C60/Ag	13.09	72
1,4-DBrB	$MAPbI_{3-x}Cl_x$	ITO/ PEDOT:PSS/Perovskite/$PC_{61}BM$/Bis-C60/Ag	12.88	72
1,4-DClB	$MAPbI_{3-x}Cl_x$	ITO/ PEDOT:PSS/Perovskite/$PC_{61}BM$/Bis-C60/Ag	11.76	72
HBr	$MAPbBr_3$	FTO/ bl-TiO_2/Perovskite /PIF8-TAA /Au	10.4	73
H_2O	$MAPbBr_3$	FTO/ bl-TiO_2/Perovskite/P3HT /Au	6.3	73
HI	$FAPbI_3$	FTO/ bl-TiO_2/Perovskite / Spiro-OMeTAD /Au	14.2	74
PEOXA	$MAPbI_3$	ITO/PEDOT:PSS/Perovskite/$PC_{61}BM$/Al	6.35	75
CHP	$MAPbI_3$	ITO/PEDOT:PSS/Perovskite/$PC_{61}BM$/Al	10.0	76
5-AVA	$(5\text{-AVA})_x(MA)_{1-x}PbI_3$	FTO/ bl-TiO_2/mp- TiO_2:Perovskite/mp-ZrO_2:Perovskite/Carbon	12.8	88

3. Sequential Deposition Method

A new route for fabricating the PSCs was proposed by Grätzel et al with an impressive high PCE of 15%, called as sequential deposition method (Figure 3).[35] This route involves firstly spin-coating of lead halide on the substrate, after drying, followed by dipping the precursor film into a solution of organoammonium halide to accomplish the conversion in a minute. (To differentiate from other two-step method, the sequential deposition in this review specifically represented this spin-coating then dipping method). Usually, a solution of 1M PbI_2 in DMF was used to fabricate the precursor film and 10 mg/mL or 8 mg/mL MAI in isopropanol (IPA) was used for dipping. The excess MAI was rinsed by IPA after the dipping step. By this method, the homogeneity of the films can be dramatically improved and the morphology can be easier controlled compared to the one-step spin-coating method.[35,89] Figure 6 exhibited the representative SEM images of the perovskite crystals by sequential deposition.

Q. Meng et al modified this method by a repeated deposition of PbI_2, and the high PCE of 10% for the mesocopic PSC without HTM was attributed to a completely covered capping layer.[90] L. Han et al employed strong coordinative DMSO as the solvent to retard the crystallization of PbI_2, leading to a more uniform precursor film as well as the resultant perovskite film with narrow crystal size distribution. The standard deviation of device efficiency is only 0.57 from 120 cells, much lower than that using DMF, revealing a higher reproducibility.[91] The concentration of MAI is another factor to affect the morphology and the electronic property of the perovskite.[92] A higher concentration of MAI solution can result in an increased I ions and a decreased hole density in the perovskite films. As a result, carrier density and charge transport ability decreased with the poorer device performance. Similarly, increasing the polarity of the solvent could have a positive effect on cell performance.[92] G. Bochloo claimed that some $MAPbI_3$ would dissolve in IPA during the rinsing step, and a treatment of dichloromethane can carry the IPA away rapidly and dry the film uniformly.[93] The treatment is conducive to the efficiency and reproducibility.

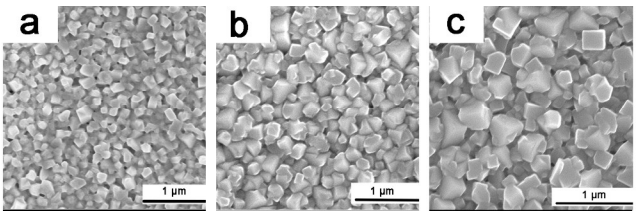

Figure 5. The representative SEM images of the perovskite crystals by sequetial deposition a) without prewetting step, b) with prewetting step and c) reacting at a high temperature. (Reproduced from Ref. 89 with permission from The Royal Society of Chemistry)

A prewetting step before dipping was pointed out to be essential for a high photogenerated current by Grätzel et al.[35] Our previous work also confirmed this conclusion.[89] A little amount of solvent IPA would remain on the surface of the PbI_2 after prewetting, so the MAI solution was slightly diluted on the solution-solid interface with a reduced nuclei density. As a result, the larger crystallites were formed with strong light scattering effect. L. Zheng et al also found that when reacting in a hot MAI solution (50°C), with a higher rate of grain boundaries' migration, the crystal size could be enlarged without reducing the coverage of the capping layer (Figure 5). Therefore, enhanced absorption caused by the strong light scattering and improved transporting properties of the large crystal greatly benefited the ultimate device performance.

To extend the carrier diffusion length by partial substitution of Cl, Y. Ma et al firstly reported the synthesis of $MAPbI_{3-x}Cl_x$ by sequential deposition using a mixture of PbI_2 and $PbCl_2$, the existence of the Cl in the film was confirmed by EDX analysis.[94] It was suggested the incorporation of a second halide could ameliorate the morphology.[94-97] S. G. Mhaisalkar et al optimized the molar ratio of PbI_2 and $PbCl_2$ as 9:1, the corresponding device displayed better performance than that of $MAPbI_3$.[95] T. Bein using a mixed solution of MAI and MACl for dipping, the mix halide perovskite can also be synthesized.[97]

A considerable limitation of the sequential deposition is the incompletely reaction when applied for the planar devices.[53,98] For a perovskite film deposited on a planar substrate, the pure crystal phase can only be obtained when the thickness was below 300 nm. When the thickness goes up, it is very hard for the MAI to penetrate and spread into the whole film, and the residual unreacted PbI_2 will ultimately impair the device efficiency.[98] A complete reaction may consume several hours, which is not only impractical but also in vain because the film will become extreme rough after such long reacting time.[99]

4. Two-step Spin-coating Method

Two-step spin-coating method, also called as an interdiffusion method, was proposed by J. Huang, as an improved or derived method from the sequential deposition.[53] The greatest difference is that the conversion from the lead halide to perovskite was accomplished by spin coating an upper layer of MAI on the precursor film followed by annealing at high temperature. (Figure 3) The film morphology on mesoporous TiO_2 by two-step spin-coating method is also very similar with that by sequential deposition.[49,100] The quantity of MAI deposited was accurately adjusted in terms of the PbI_2 down layer, so this method can fabricate more uniform films than that by sequential deposition, but also save materials and reduce the cost. The mechanism of two-step spin-coating can be concluded as the substitution of MAI for DMF.[100] Due to a weak interaction, the precursor film actually contains lots of DMF molecule coordinated with PbI_2, when the MAI deposited, PbI_2 firstly react with I^- as PbI_3^- then convert to perovskite in the present of MA^+, and DMF molecules evaporated during the annealing. The solvent-solute interaction accelerates the conversion and the annealing step enables the thorough reaction. N.-G. Park studied the difference of film morphology deposited by two-step spin-coating method and the traditional one-step method.[100] For one-step method, the uncontrolled precipitation of perovskite led to a large variation of morphology with incomplete coverage on TiO_2 and poor pore filling. While cubic-like perovskite crystals packed densely to full covered and infiltrated the TiO_2. M. Gräztel and N.-G. Park et al found that the perovskite grain size and the device performance by this method profoundly depend on the concentration of MAI (Figure 6a).[49] When the concentration is as low as 0.038M, the grain size is as big as 720 nm because of the low nuclei density. The grain size then decreased with the increasing concentration and nuclei density. The mesostructured device with the largest perovskite crystallites using lowest MAI concentration reached the highest PCE of 17.0% without hysteresis.[49]

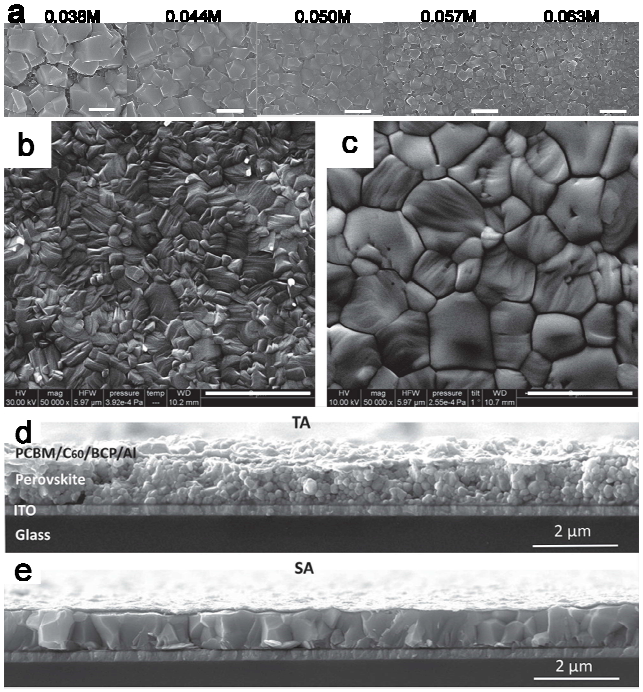

Figure 6. a) The representative SEM images of the perovskite crystallites on mesoporous TiO_2 by two-step spin-coating method with different MAI concentrations (Reproduced from Ref. 49 with permission from Nature Publishing Group). The representative SEM images of the perovskite films (thickness: 1050 nm) using two-step spin-coating method by b),d) thermal annealing and c),e) solvent annealing in the planar device. (scale bar: 2 μm) (Reproduced from Ref. 40 with permission from Wiley-VCH.)

The two-step spin-coating method is also applicable to planar devices with thick perovskite films, which is quite different from the sequential deposition. More importantly, no obvious hysteresis effect was observed in the planar device fabricated by this method with different scan direction and delay time.[40,49,53] The hysteresis effect as the recent rising hotspot shows strong dependence on different architectures, which will cause the overestimation of the PCE. It is found that much more significant hysteresis effect was observed in the planar devices and the smaller crystals rather than the meso-structured devices and the large crystals.[41] Previous researches demonstrated that

even though the hysteresis effect can be greatly improved by enlarging the crystal size, it was hard to eliminated in a planar device.[41,42,77] Surprisingly, the two-step spin-coating method seems to solve this problem. The high PCE of above 15% and the free of hysteresis effect for planar device might be attributed to the defect-free and negligible charge traps in the device. Moreover, a planar PSC with containing a 1015 nm-thick perovskite film was successfully fabricated by J. Huang et al combined with the solvent annealing technology (Figure 6).[40] The solvent (DMF) atmosphere was provided during the annealing process to accelerate the reaction between two deposited layers, also promote the grain boundary diffusion and reduce the grain boundary density. Consequently, much larger crystallites with high crystallinity formed than those by conventional thermal annealing, which connected the ETL and HTL. In another word, the most of photogenerated carriers need not go through any grain boundary before being collected. The carriers diffusion length was measured as 886 nm of $MAPbI_3$ in this device, ascribed to the quick carrier transport and extraction. High efficiency of 14.5% and 15.6% was obtained for devices with a 1015 nm-thick perovskite film and a 630 nm-thick perovskite film, respectively.[40] It is also proved that a mesoporous TiO_2 layer might not be necessary to eliminate the hysteresis effect.

5. Vapor Deposition Method

H. J. Snaith firstly reported a vapor deposition method for a planar $MAPbI_{3-x}Cl_x$ PSC by coevaporating $PbCl_2$ and MAI in the vacuum. 15.4% of PCE was achieved with narrow distribution compared to the one-step solution process.[54] Due to the difficulty on accurately controlling the ratio, the sequential vacuum deposition was developed by depositing $PbCl_2$ and MAI layer by layer.[101-102] By heating the substrate during the vapor deposition, a homogeneous pinhole-free film with pure crystal phase can be attained.[101] A high vacuum degree required in these methods is impractical and increases the cost. Y. Yang et al used a vapor-assisted solution process, in which the solution deposited PbI_2 reacted with MAI vapor on the substrate under atmospheric pressure.[55] The resultant perovskite film was composed of the microscale polycrystallines with small surface roughness corresponding to a PCE of 12%. Other vapor generated technologies like chemical vapour deposition were also used for perovskite film formation.[103,104] The most striking characteristic of morphology by such vapor deposition methods is the homogeneity, but these methods may be only applicable to the planar device.

Table 2. The characteristics of the different film forming methods.

Method	Characteristics
One-step Spin-coating	Most convenient way, need annealing. Very sensitive to the conditions, hard to control the morphology.
Sequential Deposition	Time efficient way due to very quick reaction. Uniform films with high reproducibility.
Two-step Spin-coating	Quantitatively managed method, need annealing. Uniform films with high reproducibility.
Vapor Deposition	Only used for planar devices. Very homogeneity. Vapor under vacuum: Energy consuming for high vacuum; Vapor-assisting solution process: Time consuming for annealing.

6. Conclusions and Outlook

In summary, via effective morphology control, the power conversion efficiency of the perovskite solar cells have all been boosted to above 15% by various methods. The different characteristics of each method were compared on Table 2. The sensitive dependences of PCE on the morphology were also observed. Rather than the light absorption properties, the PCEs might be more affected by the carrier transporting and collecting ability of the device. In spite of the same component or thickness, the charge transport can be quite distinct due to the different morphology. For $MAPbI_3$, previous results revealed a long charge carrier diffusion length above 100 nm in the thin film device.[15,16] After solvent annealing, reduced traps in the film increased the diffusion length to 886 nm.[40] However, updated research demonstrated a much longer diffusion length of 2-8 μm in a 100 mm^3 single crystal[105] and even reached 175 μm under 1 sun illumination in single crystals with a top-seeded solution-growth method.[106] Therefore, more investigations about the charge transport mechanism based on the different morphologies were necessary for further improving the film fabricating technique. The optimization of the other parts, for example, the component of mixed halide perovskite, should be studied and compared based on each optimized morphology, otherwise the material cannot be fully brought into play and the results might not be accurate. Moreover, there is no report yet about the relations between the film stability and the morphology, which might be crucial to the application.

Although we temporarily can't describe exactly what a most efficient morphology should be like, many hints can be achieved by the existing researches. The hysteresis effect should be used to evaluate the quality of a perovskite film, because it has a close relation with the stored charges in the film. If the charges can transport rapidly and be extracted by the electrode effectively without delay, the hysteresis effect can be inhibited or even eliminated. We noticed the "high-quality perovskite films" (both with high PCE and weak hysteresis effect) possess the similar morphology, although they were obtained by different method and treatments. Table 3 concluded the methods and the corresponding PCEs by different scan directions for the "high-quality perovskite films." As to the

meso-structured architecture, a pure perovskite capping layer with large grain size is the key. The ratio of the pure perovskite layer and the nanocomposite layer should be optimized to eliminate the hysteresis effect.[42] As to the planar architecture, firstly, the perovskite films were always composed of densely packed perovskite grains. Besides, the film thickness was above 300 nm to harvest enough light. More importantly, no grain boundaries were parallel to the substrate, which requires the crystal grain size should be bigger than the thickness of the film. Such a film can make sure that most of the photogenerated charges needn't go through the grain boundaries before reaching the electrode. Therefore, efficient transport and collection with reduced energy loss results in a high PCE and weak hysteresis. Furthermore, the p-i-n junction of PEDOT:PSS/perovskite/PCBM exhibits more superior properties than TiO_2/perovskite/HTM junction. The existence of PCBM on perovskite can passivate the trap states on the surface and grain boundaries of perovskite crystals by permeating into the grain boundaries. Therefore, the photocurrent hysteresis would be effectively eliminated with significantly reduced trap density.[107] Based on the existing method, new technology for the industrial production is becoming an urgency. Recently, the blade-coating method was extended to fabricate the planar perovskite solar cells with enhanced environmental stability.[108] A 3D printer was also exploited to fabricate a 47.3 cm^2 perovskite solar cells with 11.6% efficiency via a roll-to-roll process.[109] These should be the good start for perovskite solar cells moving towards the practical application. For the future, however, morphology control on a large scale is still a very important issue.

Table 3. A summary of the methods and the corresponding PCEs for the "high-quality perovskite films."

Method	Treatment	Device	Thickness[a] (nm)	PCE (%) (rev./forw.)	Ref.
One-step spin-coating	FDC	FTO/ bl-TiO_2/$MAPbI_3$/ Spiro-OMeTAD /Au	350	13.8/11.6	79
One-step spin-coating	Gas-assisted dry	FTO/ bl-TiO_2/$MAPbI_3$ / Spiro-OMeTAD /Au	300	17.1/16.5	80
One-step spin-coating	Solvent-engineering process	FTO/ bl-TiO_2/mp-TiO_2/$MAPb(I_{1-x}Br_x)_3$ / PTAA /Au	200/200	16.7/16.2	81
One-step spin-coating	Solvent-engineering process	ITO/ PEDOT:PSS/$MAPbI_3$/$PC_{61}BM$/Bis-C60/Ag	300	13.8/13.5	83
One-step spin-coating	Solvent-engineering process	ITO/ PEDOT:PSS/$MAPbI_3$/$PC_{61}BM$/LiF/Al	350	12.9/12.6	82
One-step spin-coating	Solvent-engineering process	FTO/ bl-TiO_2/mp- TiO_2/$(FAPbI_3)_{1-x}(MAPbBr_3)_x$/ PTAA /Au	200/300	19.0/17.8	86
One-step spin-coating	Addtion of HBr	FTO/ bl-TiO_2/$MAPbBr_3$ / PIF8-TAA /Au	500	10.4/10.4	73
One-step spin-coating	Hot-casting technique	FTO/ PEDOT:PSS/$MAPbI_{3-x}Cl_x$ /$PC_{61}BM$/Al	450	17.7/17.7	85
Two-step spin-coating	-	FTO/ bl-TiO_2/mp- TiO_2/$MAPbI_3$/Spiro-OMeTAD /Au	100/300-400	17.0/-	49
Two-step spin-coating	-	ITO/ PEDOT:PSS/$MAPbI_3$/$PC_{61}BM$/C_{60}/BCP/Al	270-300	15.4/15.4	53
Two-step spin-coating	Solvent annealing	ITO/ PEDOT:PSS/$MAPbI_3$/$PC_{61}BM$/C_{60}/BCP/Al	630	15.6/15.6	40

[a] The thickness of pure perovskite, or nanocomposite/capping layer if a mesostructured solar cell.

Acknowledgements

This study was partly financially supported by the National Natural Science Foundation of China (61177020 and 11121091) and the National Basic Research Program of China (2013CB328700). The authors are thankful to Mr. Zhengpeng Li of the University of Texas and Mr. Peng Chen of Peking University for helpful discussions.

Notes and references

[a] State Key Laboratory for Mesoscopic Physics and Department of Physics, Peking University, [b]Beijing Engineering Research Center for Active Matrix Display, Beijing 100871, China
[c] New Display Device and System Integration Collaborative Innovation Center of the West Coast of the Taiwan Strait, Fuzhou 350002, China

1 D. B. Mitzi, *J. Mater. Chem.,* 2004, **14,** 2355-2365.
2 D. B. Mitzi, C. A. Feild, W. T. A. Harrison and A. M. Guloy, *Nature,* 1994, **369,** 467-469.
3 D. B. Mitzi, *J. Chem. Soc., Dalton Trans.,* 2001, **1,** 1–12.
4 C. C. Stoumpos, C. D. Malliakas and M. G. Kanatzidis, *Inorg. Chem.,* 2013, **52,** 9019-9038.
5 W.-J. Yin, J.-H. Yang, J. Kang, Y. Yan and S.-H. Wei, *J. Mater. Chem. A,* 2015, DOI: 10.1039/C4TA05033A.
6 P. Gao, M. Gräztel and M. K. Nazeeruddin, *Energy Environ. Sci.,* 2014, **7,** 2448-2463.
7 T. Baikie, Y. Fang, J. M. Kadro, M. Schreyer, F. Wei, S. G. Mhaisalkar, M. Gräztel and T. J. White, *J. Mater. Chem. A,* 2013, **1,** 5628-5641.
8 S. A. Bretscheider, J. Weickert, J. A. Dorman and L. Schmidt-Mende, *APL Materials,* 2014, **2,** 040701.
9 S. Colella, E. Mosconi, P. Fedeli, A. Listorti, F. Gazza, F. Orlandi, P. Ferro, T. Besagni, A. Rizzo, G. Calestani, G. Gigli, F. D. Angelis and R. Mosca, *Chem. Mater.,* 2013, **25,** 4613-4618.
10 F. Hao, C. C. Stoumpos, R. P. H. Chang and M. G. Kanatzidis, *J. Am. Chem. Soc.,* 2014, **136,** 8094−8099.
11 Yoshino, S. S. Pandey, T. Ma and S. Hayase, *J. Phys. Chem. Lett.,* 2014, **5,** 1004−1011.

12 F. Zuo, S. T. Williams, P.-W. Liang, C.-C. Chueh, C.-Y. Liao and A. K.-Y. Jen, *Adv. Mater.,* 2014, **26,** 6454-6460.
13 F. Hao, C. C. Stoumpos, D. H. Cao, R. P. H. Chang and M. G. Kanatzidis, *Nature Photonics,* 2014, **8,** 489-494.
14 N. K. Noel, S. D.Stranks, A. Abate, C. Wehrenfennig, S. Guarmera, A. A. Haghighirad, A. Sadhanala, G. E. Eperson, M. B. Johnston, A. M. Petrozza, L. M. Herz, H. J. Snaith, *Energy Environ. Sci.,* 2014, **7,** 3061-3068.
15 S. D. Stranks, G. E. Eperon, G. Grancini, C. Menelaou, M. J. P. Alcocer, T. Leijtens, L. M. Herz, A. Petrozza and H. J. Snaith, *Science,* 2013, **342,** 341−344.
16 G. Xing, N. Mathews, S. Sun, S. S. Lim, Y. M. Lam, M. Gräztel, S. Mhaisalkar and T. C. Sum, *Science,* 2013, **342,** 344−347.
17 C. S. Ponseca Jr, T. J. Savenije, M. Abdellah, K. Zheng, A. Yartsev, T. Pascher, T. Harlang, P. Chabera, T. Pullerits, A. Stepanov, J.-P. Wolf and V. Sundström, *J. Am. Chem. Soc.,* 2014, **136,** 5189–5192.
18 Q. Lin, A. Armin, R. C. R. Nagiri, P. L. Burn and P. Meredith, *Nature Photonics,* 2014, **284,** 1-7.
19 A. Kojima, K. Teshima, Y. Shirai and T. Miyasaka, *J. Am. Chem. Soc.,* 2009, **131,** 6050-6051.
20 P. P. Boix, K. Nomomura, N. Mathews and S. G. Mhaisalkar, *Materials Today,* 2014, **17,** 16-23.
21 N.-G. Park, *Materials Today,* 2014, DOI:10.1016/j.mattod.2014.07.007.
22 S. Kazim, M. K. Nazeeruddin, M. Gräztel and S. Ahmad, *Angew. Chem. Int. Ed.,* 2014, **53,** 2812-2824.
23 T. C. Sum and N. Mathews, *Energy Environ. Sci.,* 2014, **7,** 2518.
24 S. Gamliel and L. Etgar, *RSC Adv.,* 2014, **4,** 29012.
25 B. Wang, X. Xiao and T. Chen, *Nanoscale,* 2014, **6,** 12287-12297.
26 J. Yan and B. R. Saunders, *RSC Adv.,* 2014, **4,** 43286.
27 S. Luo and W. A. Daoud, *J. Mater. Chem. A,* 2015, DOI: 10.1039/C4TA04953E.
28 H. J. Snaith, *J. Phys. Chem. Lett.*, 2013, **4,** 3623-3630.
29 H.-S. Kim, S. H. Im and N.-G. Park, *J. Phys. Chem. C,* 2014, **118,** 5615−5625.
30 M. A. Green, A. Ho-Baillie and H. J. Snaith, *Nature Photonics,* 2014, **8,** 506.
31 Y. Ma, S. Wang, L. Zheng, Z. Lu, D. Zhang, Z. Bian, C. Huang and L. Xiao, *Chin. J. Chem.,* 2014, **32,** 957-963.
32 H.-S. Kim, C. R. Lee, J. H. Im, K. B. Lee, T. Moehl, A. Marchioro, S. J. Moon, R. Humphry-Baker, J. H. Yum, J. E. Moser, M. Gräztel and N. G. Park, *Sci. Rep.,* 2012, **2,** 591.
33 M. M. Lee, J. Teuscher, T. Miyasaka, T. N. Murakami and H. J. Snaith, *Science,* 2012, **338,** 643−647.
34 G. E. Eperon, V. M. Burlakov, P. Docampo, A. Goriely and H. J. Snaith, *Adv. Funct. Mater.,* 2014, **24,** 151-157.
35 J. Burschka, N. Pellet, S.-J. Moon, R. Humphry-Baker, P. Gao, M. K. Nazeeruddin and M. Gräztel, *Nature,* 2013, **499,** 316−319.
36 H. Zhou, Q. Chen, G. Li, S. Luo, T. Song, H.-S. Duan, Z. Hong, J. You, Y. Liu and Y. Yang, *Science,* 2014, **345,** 542.
37 http://www.nrel.gov
38 A. Dualeh, N. Tétreault, T. Moehl, P. Gao, M. K. Nazeeruddin and M. Grätzel, *Adv. Funct. Mater.*, 2014, **24**, 3250.
39 Y. Zhao and K. Zhu, *J. Phys. Chem. Lett.*, 2014, **5,** 4175-4186.
40 Z. Xiao, Q. Dong, C. Bi, Y. Shao, Y. Yuan and J. Huang, *Adv. Mater.,* 2014, **26,** 6503.
41 H.-S. Kim and N.-G. Park, *J. Phys. Chem. Lett.*, 2014, **5,** 2827-2934.
42 E. L. Unger, E. T. Hoke, C. D. Bailie, W. H. Nguyen, A. R. Bowring, T. Heumüller, M. G. Christoforo and M. D. McGehee, *Energy Environ. Sci.,* 2014, **7,** 3690-3698.
43 H. J. Snaith, A. Abate, J. M. Ball, G. E. Eperon, T. Leijtens, N. K. Noel, S. D. Stranks, J. T.-W. Wang, K. Wojciechowski and W. Zhang, *J. Phys. Chem. Lett.*, 2014, **5,** 1511-1515 .
44 R. S. Sanchez, V. Gonzalez-Pedro, J.-W. Lee, N.-G. Park, Y. S. Kang, I. Mora-Sero and J. Bisquert, *J. Phys. Chem. Lett.,* 2014, **5,** 2357−2363.
45 J. Wei, Y. Zhao, H. Li, G. Li, J. Pan, D. Xu, Q. Zhao and D. Yu, *J. Phys. Chem. Lett.,* 2014, **5,** 3937−3945.
46 J. M. Ball, M. M. Lee, A. Hey and H. J. Snaith, *Energy Environ. Sci.,* 2013, **6,** 1739.
47 N. Li, H. Dong, H. Dong, J. Li, W. Li, G. Niu, X. Guo, Z. Wu and L. Wang, *J. Mater. Chem. A,* 2014, **2,** 14973.
48 T. Leijtens, B. Lauber, G. E. Eperson, S. D. Stranks and H. J. Snaith, *J. Phys. Chem. Lett.,* 2014, **5,** 1096-1102.
49 J.-H. Im, I.-H, Jang, N. Pellet, M. Grätzel and N.-G. Park, *Nature Nanotechnology,* 2014, **9,** 927-932.
50 P.-W. Liang, C.-Y. Liao, C.-C.Chueh, F. Zuo, S. T. Williams, X.-K. Xin, J. Lin and A. K.-Y. Jen, *Adv. Mater.,* 2014, **26,** 3748–3754.
51 Y. Zhao and K. Zhu, *J. Phys. Chem. C,* 2014, **118,** 9412-9418.
52 M. Saliba, K. W. Tan, H. Sai, D. T. Moore, T. Scott, W. Zhang, L. A. Estroff, U. Wiesner and H. J. Snaith, *J. Phys. Chem. C,* 2014, **118,** 17171-17177.
53 Z. Xiao, C. Bi, Y. Shao, Q. Dong, Q. Wang, Y. Yuan, C. Wang, Y. Gao and J. Huang, *Energy Environ. Sci.,* 2014, **7,** 2619.
54 M. Liu, M. B. Johnston and H. J. Snaith, *Nature,* 2013, **501,** 395.
55 Q. Chen, H. Zhou, Z. Hong, S. Luo, H.-S. Duan, H.-H. Wang, Y. Liu, G. Li and Y. Yang, *J. Am. Chem. Soc.,* 2013, **136,** 622-625.
56 Q. Wang, Y. Shao, Q. Dong, Z. Xiao, Y. Yuan and J. Huang, *Energy Environ. Sci.,* 2014, **7,** 2359.
57 D. Shen, X. Yu, X. Cai, M. Peng, Y. Ma, X. Su, L. Xiao and D. Zou, *J. Mater. Chem. A,* 2014, **2,** 20454.
58 S. Paek, N. Cho, H. Choi, H. Jeong, J. S. Lim, J.-Y. Hwang, J. K. Lee and J. Ko, *J. Phys. Chem. C,* 2014, **118,** 25899-25905.
59 H.-B. Kim, H. Choi, J. Jeong, S. Kim, B. Walker, S. Song and J. Y. Kim, *Nanoscale,* 2014, **6,** 6679.
60 E. Mosconi, A. Amat, M. K. Nazeeruddin, M. Grätzel and F. D. Angelis, *J. Phys. Chem. C,* 2013, **117,** 13902-13913.
61 J. H. Noh, S. H. Im, J. H. Heo, T. N. Mandal and S. I. Seok, *Nano Lett.,* 2013, **13,** 1764−1769.
62 J.-Y. Jeng, Y.-F. Chiang, M.-H. Lee, S.-R. Peng, T.-F. Guo, P. Chen and T.-C. Wen, *Adv. Mater.,* 2013, **25,** 3727-3732.
63 R. Kang, J.-E. Kim, J.-S. Yeo, S. Lee, Y.-J. Jeon and D.-Y. Kim, *J. Phys. Chem. C,* 2014, **118,** 26513-26520.
64 S. Chavhan, O. Miguel, H.-J. Grande, V. Gonzalez-Pedro, R. S. Sánchez, E. M. Barea, I. Mora-Seró and R. Tena-Zaera, *J. Mater. Chem. A,* 2014, **2,** 12754-12760.
65 J.-Y. Jeng, K.-C. Chen, T.-Y. Chiang, P.-Y. Lin, T.-D. Tsai, Y.-C. Chang, T.-F. Guo, P. Chen, T.-C. Wen and Y.-J. Hsu, *Adv. Mater.,* 2014, **26,** 4107-4113.
66 J. You, Y. Yang, Z. Hong, T.-B. Song, L. Meng, Y. Liu, C. Jiang, H. Zhou, W.-H. Chang, G. Li and Y. Yang, *Appl. Phys. Lett.,* 2014, **105,** 183902.

67 Z. Ren, A. Ng, Q. Shen, H. C. Gokkaya, J. Wang, L. Yang, W.-K. Yiu, G. Bai, A. B. D. Djurišić, W. W. Leung, J. Hao, W. K. Chan and C. Surya, *Sci. Rep.,* 2014, **4,** 6752.
68 Y. Guo, C. Liu, K. Inoue, K. Harano, H. Tanaka and E. Nakamura, *J. Mater. Chem. A,* 2014, **2,** 13827-13830.
69 S. Aharon, A. Dymshits, A. Rotem and L. Etgar, *J. Mater. Chem. A,* 2015, DOI: 10.1039/C4TA05149A.
70 S. Lv, S. Pang, Y. Zhou, N. P. Padture, H. Hu, L. Wang, X. Zhou, H. Zhu, L. Zhang, C. Huang and G. Cui, *Phys. Chem. Chem. Phys.,* 2014, **16,** 19206-19211.
71 C. Zuo and L. Ding, *Nanoscale,* 2014, **6,** 9935.
72 C.-C. Chueh, C.-Y. Liao, F. Zuo, S. T. Williams, P.-W. Liang and A. K.-Y. Jen, *J. Mater. Chem. A,* 2015, DOI: 10.1039/C4TA05012F.
73 J. H. Heo, D. H. Song and S. H. Im, *Adv. Mater.,* 2014, DOI: 10.1002/adma.201403140
74 G. E. Eperson, S. D. Stranks, C. Menelaou, M. B. Johnston, L. M. Herz and H. J. Snaith, *Energy Environ. Sci.,* 2014, **7,** 982-988.
75 Q. Xue, Z. Hu, C. Sun, Z. Chen, Fei. Huang, H.-L. Yip and Y. Cao, *RSC Adv.,* 2015, **5,** 775.
76 Y.-J. Jeon, S. Lee, R. Kang, J-E, Kim, J.-S. Yeo, S.-H. Lee, S.-S. Kim, J.-M. Yun and D.-Y. Kim, *Scientific Reports*, 2014, **4,** 6953.
77 M. Gräztel, *Nature Materials,* 2014, **13,** 838-842.
78 F. Liu, J. Zhu, J. Wei, Y. Li, M. Lv, S. Yang, B. Zhang, J. Yao and S. Dai, *Appl. Phys. Lett.,* 2014,**104,** 253508.
79 M. Xiao, F. Huang, W. Huang, Y. Dkhissi, J. Etheridge, A. Gray-Weale, U. Bach, Y.-B. Cheng and L. Spiccia, *Angew. Chem. Int. Ed.,* 2014, **53,** 9898 –9903.
80 F. Huang, Y. Dkhissi, W. Huang, M. Xiao, I. Benesperi, S. Rubanov, Y. Zhu, X. Lin, L. Jiang, Y. Zhou, A. Gray-Weale, J. Etheridge, C. R. McNeill, R. A. Caruso, U. Bach, L. Spiccia and Y.-B. Cheng, *Nano Energy,* 2014, **10,** 10-18.
81 N. J. Jeon, J. H. Noh, Y. C. Kim, W. S. Yang, S. Ryu and S. I. Seok, *Nature Materials,* 2014, **13,** 897-903.
82 J. Seo, S. Park, Y. C. Kim, N. J. Jeon, J. H. Noh, S. C. Yoon and S. I. Seok, *Energy Environ. Sci.,* 2014, **7,** 2642.
83 J. W. Jung, S. T. Williams and A. K.-Y. Jen, *RSC Adv.,* 2014, **4,** 62971.
84 J. Cui, F. Meng, H. Zhang, K. Cao, H. Yuan, Y. Cheng, F. Huang and M. Wang, *ACS Appl. Mater. Interfaces,* 2014, **6,** 9711−9718.
85 W. Nie, H. Tsai, R. Asadpour, J.-C. Blancon, A. J. Neukirch, G. Gupta, J. J. Crochet, M. Chhowalla, S. Tretiak, M. A. Alam, H.-L. Wang and A. D. Mohite, *Science,* 2015, **347,** 522-525.
86 N. J. Jeon, J. H. Noh, W. S. Yang, Y. C. Kim, S. Ryu, J. Seo and S. I. Seok, *Nature,* 2015, **517,** 476-480.
87 Y. Ogomi, A. Morita, S. Tsukamoto, T. Saitho, Q. Shen, T. Toyoda, K. Yoshino, S. S. Pandey, T. Ma and S. Hayase, *J. Phys. Chem. C,* 2014, **118,** 16651-16659.
88 A. Mei, X. Li, L. Liu, Z. Ku, T. Liu, Y. Rong, M. Xu, M. Hu, J. Chen, Y. Yang, M. Gra and H. Han, *Science,* 2014, **345,** 295.
89 L. Zheng, Y. Ma, S. Chu, S. Wang, B. Qu, L. Xiao, Z. Chen, Q. Gong, Z. Wu and X. Hou, *Nanoscale,* 2014, **6,** 8171-8176.
90 J. Shi, Y. Luo, H. Wei, J. Luo, J. Dong, S. Lv, J. Xiao, Y. Xu, L. Zhu, X. Xu, H. Wu, D. Li and Q. Meng, *ACS Appl. Mater. Interfaces,* 2014, DOI: 10.1021/am507108u.
91 Y. Wu, A. Islam, X. Yang, C. Qin, J. Liu, K. Zhang, W. Peng and L. Han, *Energy Environ. Sci.,* 2014, **7,** 2934.
92 J. Shi, H. Wei, S. Lv, X. Xu, H. Wu, Y. Luo, D. Li and Q. Meng, ChemPhysChem, DOI: 10.1002/cphc.201402815.
93 D. Bi, A. M. El-Zohry, A. Hagfeldt and G. Boschloo, 2014, *ACS Appl. Mater. Interfaces,* DOI: 10.1021/am504320h.
94 Y. Ma, L. Zheng, Y.-H. Chung, S. Chu, L. Xiao, Z. Chen, S. Wang, B. Qu, Q. Gong, Z. Wu and X. Hou, *Chem. Commun.,* 2014, **50,** 12458-12461.
95 S. Dharani, H. A. Dewi, R. R. Prabhakar, T. Baikie, C. Shi, D. Yonghua, N. Mathews, P. P. Boix and S. G. Mhaisalkar, *Nanoscale,* 2014, **6,** 13854-13860.
96 M. Jiang, J. Wu, F. Lan, Q. Tao, D. Gao and G. Li. *J. Mater. Chem. A,* 2015, DOI: 10.1039/C4TA05373G.
97 P. Docampo, F. Hanusch, S. D. Stranks, M. Döblinger, J. M. Feckl, M. Ehrensperger, N. K. Minar, M. B. Johnston, H. J. Snaith, T. Bein, *Adv. Energy Mater.,* 2014, **4,** 1400355.
98 D. Liu, M. K. Gangishetty and T. L. Kelly, *J. Mater. Chem. A,* 2014, **2,** 19873-19881.
99 K. Liang, D. B. Mitzi and M. T. Prikas, *Chem. Mater.,* 1998, **10,** 403-411.
100 J.-H. Im, H.-S. Kim and N.-G. Park, *APL Materials,* 2014, **2**, 081510.
101 C.-W. Chen, H.-W. Kang, S.-Y. Hsiao, P.-F. Yang, K.-M. Chiang and H.-W. Lin, *Adv. Mater.,* 2014, DOI: 10.1002/adma.201402461.
102 H. Hu, D. Wang, Y. Zhou, J. Zhang, S. Lv, S. Pang, X. Chen, Z. Liu, N. P. Padture and G. Cui, *RSC Adv.,* 2014, **4,** 28964-28967.
103 M. R. Leyden, L. K. Ono, S. R. Raga, Y. Kato, S. Wang and Y. Qi, *J. Mater. Chem. A,* 2014, **2,** 18742.
104 F. Hao, C. C. Stoumpos, Z. Liu, R. P. H. Chang and M. G. Kanatzidis, *J. Am. Chem. Soc.,* 2014, **136,** 16411-16419.
105 D. Shi, V. Adinolfi, R. Comin, M. Yuan, E. Alarousu, A. Buin, Y. Chen, S. Hoogland, A. Rothenberger, K. Katsiev, Y. Losovyj, X. Zhang, P. A. Dowben, O. F. Mohammed, E. H. Sargent and O. M. Bakr, *Science,* 2015, **347,** 519.
106 Q. Dong, Y. Fang, Y. Shao, P. Mulligan, J. Qiu, L. Cao and J. Huang, *Science,* 2015, DOI:10.1126/science.aaa5760.
107 Y. Shao, Z. Xiao, C. Bi, Y. Yuan and J. Huang, *Nature Communications,* 2014, **5,** 5784.
108 J. H. Kim, S. T. Williams, N. Cho, C.-C. Chueh and A. K.-Y. Jen, *Adv. Energy Mater.*, 2014, DOI: 10.1002/aenm.201401229.
109 D. Vak, K. Hwang, A. Faulks, Y.-S. Jung, N. Clark, D.-Y. Kim, G. J. Wilson and S. E. Watkins, *Adv. Energy Mater.*, 2014, DOI: 10.1002/aenm.201401539.